Optimal Parameters and Placement of Hybrid Energy Storage Systems for Frequency Stability Improvement

Dan Liu, Qiufan Yang, Yin Chen, Xia Chen, *Senior Member*, *IEEE,* and Jinyu Wen, *Member*, *IEEE*

***Abstract*—Energy storage with virtual inertia and virtual droop control has attracted wide attention due to its improved frequency stability with high penetration of renewable energy sources. However, there are significant spatial differences in frequency response. The location and capacity of energy storage are urgent issues to be resolved to support frequency. This study addresses the minimum investment of hybrid energy storage systems for providing sufficient frequency support, including the power capacity, energy capacity, and location of energy storage. A frequency response model is developed taking into account the network structure and frequency spatial distribution characteristics. In addition, a numerical computation method is provided for determining the frequency dynamic indices and calculating the output power of energy storage. Based on a simplified frequency response model, an optimal hybrid energy storage configuration method is proposed to optimize the control parameters, location, and capacity to satisfy the frequency dynamic constraints. This configuration method can exploit the potential of energy storage with different rates in different frequency support stages. To address the nonconvex drawback of this configuration, a numerical calculation method is provided based on the explicit gradient of the frequency and energy storage indices to enhance the computational efficiency. Simulations of a two-area system and the south-east Australian system verify the effectiveness of the proposed hybrid energy storage configuration method.**

***Index Terms*—Hybrid energy storage, inertia control, droop control, optimal configuration, frequency stability.**

Received: March 20, 2024
Accepted: August 28, 2024
Published Online: March 1, 2025

Dan Liu is with the School of Electrical and Electronic Engineering, Huazhong University of Science and Technology, Wuhan 430074, China, and the State Grid Hubei Electric Power Research Institute, Wuhan 430000, China (e-mail: danliu6@hust.edu.cn).

Qiufan Yang, Xia Chen, and Jinyu Wen are with the State Key Laboratory of Advanced Electromagnetic Technology, and the School of Electrical and Electronic Engineering, Huazhong University of Science and Technology, Wuhan 430074, China (e-mail: yangqiufan@hust.edu.cn; cxhust@foxmail.com; jy.wen@hust.edu.cn).

Yin Chen (corresponding author) is with the Department of Electronic and Electrical Engineering, University of Strathclyde, Glasgow G11XW, UK (e-mail: yin.chen.101@strath.ac.uk).

DOI: 10.23919/PCMP.2023.000259

I. Introduction

With massive converter-interfaced renewable sources replacing synchronous generators, there is growing concern about the frequency stability of the power system [1], [2]. Unlike synchronous generators, no rotor or governor is directly connected to the grid frequency in renewable sources, resulting in a system with low-level inertia and damping features. The fluctuations in the output power of renewable sources lead to a growing number of frequency incidents [3], [4].

To prevent frequency safety incidents, several studies have been conducted on power system optimization that consider frequency safety [5]–[9]. These studies focus on economic dispatch and unit combinations to deal with frequency safety incidents by changing the starting mode of the units and optimizing the frequency regulation reserve. However, the transmission capacity and network topology limit the starting mode of the units and indirectly affect the frequency modulation capability of the system. There have also been some studies on transmission line planning for improving frequency stability [10], [11]. Although the frequency-regulation potential can be fully exploited through a unit combination and optimal dispatch, frequency-regulation resources are depleted with the increasing proportion of new energy sources.

As a flexible resource that can be adjusted bidirectionally, configuring energy storage is an efficient method for maintaining frequency stability. Various control methods for energy storage systems have been proposed to improve the inertia and damping of these systems [12]–[14]. Virtual inertia and droop control are the most widely adopted basic control methods for energy storage participation in frequency support [15]. Grid operators are more concerned about the amount of energy storage that must be deployed to satisfy the frequency dynamic safety constraints. To improve inertia and primary frequency reserves, a method for sizing energy storage by quantitatively describing the contribution of energy storage to inertia and droop is

proposed [16]. Considering the constraint of the rate of change of frequency (RoCoF) and frequency nadir, a linearization technique is adopted in [17] to optimize the location and sizing of energy storage. To deal with the variability of renewable energy resources, an estimation of the inertia of the system is proposed in [18] using probability distributions of generator outages.

These configuration and optimization operation methods to improve the frequency stability are based on the assumption that the frequency of each node of the system is consistent during dynamics. However, the dynamic frequency response of each node has a different spatial distribution [19]. The frequency response models adopted in [16]–[18] can only represent the average frequency dynamics of the system, which may lead to individual node frequencies not satisfying the frequency constraints. To consider the node frequency, reference [20] uses the $\mathcal{H}_2$ norm, which describes the network consistency as the optimization objective for the placement of inertia. Matrix perturbation theory is applied in [21] to obtain the optimal inertia and primary control positions. Considering the explicit time-domain constraints on frequency, the optimal placement of inertia and damping in the system is proposed by optimizing the eigenvalues of the system [22]. Nonetheless, these studies focus on the configuration of the inertia and droop coefficients from the control perspective, whose optimization objectives are related to the frequency stability index, such as the $\mathcal{H}_2$ norm, eigenvalue damping ratio, and so on. To achieve better frequency stability, these configuration methods may yield costly results. In [23], the energy storage cost and frequency dynamic indices are considered as the optimization objective and constraints, respectively, to optimize the allocation of the energy storage system. A linearized approximation is used to convert the techno-economic optimization problem into an optimization of the inertia coefficients of each node. Although this method allows for a very simple and fast configuration of energy storage, considering the differences in the node frequency response, this linearized approach is only suitable for relatively small perturbations and not for systems with significant power shortages.

Hybrid energy-storage systems combine energy-storage systems with high power and energy densities and provide frequency support services on different timescales [24]. The controller values for the hybrid energy storage systems are set using the multi-objective optimization method [25]. A multifilter-based dynamic power-sharing control strategy for a hybrid energy storage system is proposed in [26] to smooth the power fluctuations. These studies of energy storage systems mainly focus on controller design rather than investment in energy storage systems. However, the controller parameters and the configured energy storage capacity are mutually restricted. A larger controller parameter implies better frequency support, but more power and energy are required. Hence, the control parameters for hybrid energy storage must be optimized when configuring the energy storage system to support frequency performance.

To bridge the gap between the optimal frequency control and the energy capacity limit, the Gaussian pseudospectral method is adopted in [27] to optimize the power output and parameter tuning of the synthetic inertia control. However, frequency security constraints during the frequency response are ignored. In [28], considering the frequency nadir constraint, the optimal control problem of the energy storage system's minimum energy demand for frequency regulation is transformed into an optimal frequency trajectory planning problem. An analytical expression for the minimum energy demand required to ensure a sufficient frequency response is derived. However, the constraints of the RoCoF and quasi-steady-state frequency are ignored.

1) Spatial difference in frequency response: Most existing studies assume that the frequency is a global variable that maintains consistency across all parts of a power system. However, the placement of frequency resources has a significant influence on frequency stability. Hence, it is necessary to characterize indicators such as the nadir and RoCoF for different nodes.

2) Response time difference: this is a crucial parameter for energy storage to provide frequency regulation. It varies significantly among different types of energy storage systems. Most studies that consider inertia support often overlook the magnitude of the response time. However, the response time significantly influences the size of the energy storage.

3) Control parameter and capacity demand: existing literature typically configures energy storage systems by specifying frequency control parameters. However, the control parameters should be constrained by the capacity limit of the energy storage. It is unclear how to set the control parameters for different types of energy storage and allocate their frequency-regulation power to the capacity limit.

To address these challenges, a novel hybrid energy storage system configuration method is proposed to constrain the frequency dynamics within allowable limits. The original optimal placement and capacity problem for energy storage was formulated as an optimal control parameter problem of the energy storage that ensures sufficient frequency support. It should be emphasized that the optimal control parameters, size, and placement of energy storage systems can be determined simultaneously. The main contributions of the proposed configuration method are summarized as follows.

1) To address the limitations in the existing literature that fail to consider the spatial characteristics of frequency response and the impact of response speed from

different types of energy storage on energy storage configuration, this study establishes a node frequency response model incorporating various types of energy storage based on state-space representation. In addition, this study provides numerical calculation methods for frequency indicators. Compared with [23] using a linearized approximation, the simplified frequency response model established in this study can calculate the frequency dynamics more accurately.

2) In the current literature, there is a problem where energy storage configuration is determined based on the given frequency control parameters without allocating power among different types of energy storage. This study introduces a configuration method that optimizes energy storage control parameters according to economic principles and allocates frequency regulation power among different types of energy storage.

3) The optimization solving speed is considerably slow because of the nonconvex nature of the configuration model and the absence of an established analytical expression between the objective function and configuration variables. To enhance computational efficiency, a numerical computation method based on explicit gradients derived from frequency and energy storage indicators is proposed.

The remainder of this paper is organized as follows. Section II describes the simplified frequency-response model of the system with hybrid energy storage, while Section III illustrates the proposed hybrid energy storage numerical configuration algorithm and provides an explicit gradient calculation method. Section IV presents case studies to validate the effectiveness of the proposed configuration method under different application scenarios. Finally, Section V provides the conclusions.

II. Frequency Response Model

To enhance frequency stability and constrain frequency dynamics within permissible limits, it is necessary to establish a frequency analysis model. Regarding the optimization problem, the complex frequency response model is difficult to solve, whereas the simple frequency response model can lead to a loss of accuracy. Hence, in this section, a simple frequency response model is established that considers the spatial frequency distribution characteristics by extracting the key links of the frequency response in the system.

A. Thermal Generator

The swing equation dynamic of the rotor for the thermal generator is given by:

$$m_i\Delta\dot{\omega}_i + d_i\Delta\omega_i = \Delta u_i + \Delta p_{\mathrm{m}i} - \Delta p_{ei} \tag{1}$$

where m_i is the inertia of the rotor; d_i is the damping of the rotor; Δu_i is the outside disturbance; $\Delta\omega_i$ is the variation of the rotor angular frequency; $\Delta p_{\mathrm{m}i}$ is the variation of the mechanical power; and Δp_{ei} is the variation of the electromagnetic power.

The model of the intermediate reheat turbine adopted in the speed control system of the thermal power unit is as follows:

$$\begin{cases} T_{\mathrm{G}i}\Delta\dot{\mu}_i = -\Delta\omega_i / R_i - \Delta\mu_i \\ T_{\mathrm{CH}i}\Delta\dot{p}_{\mathrm{HP}i} = \Delta\mu_i - \Delta p_{\mathrm{HP}i} \\ T_{\mathrm{RH}i}\Delta\dot{p}_{\mathrm{RH}i} = \Delta p_{\mathrm{HP}i} - \Delta p_{\mathrm{RH}i} \\ \Delta p_{\mathrm{m}i} = F_{\mathrm{HP}i}\Delta p_{\mathrm{HP}i} + (1 - F_{\mathrm{HP}i})\Delta p_{\mathrm{RH}i} \end{cases} \tag{2}$$

where $T_{\mathrm{G}i}$, $T_{\mathrm{CH}i}$, and $T_{\mathrm{RH}i}$ are the time constants of the governor, steam chest, and reheater, respectively; F_{HP_i} is the fraction of total turbine power generated by the high-pressure cylinder; R_i is the adjustment factor for the governor; $\Delta\mu_i$ is the variation of the valve position; $\Delta p_{\mathrm{HP}i}$ is the variation of the output power for the high-pressure cylinder; and $\Delta p_{\mathrm{RH}i}$ is the variation of the output power for the reheater.

B. Hybrid Energy Storage

The frequency response model of the energy storage system actively participating in frequency support is shown in Fig. 1.

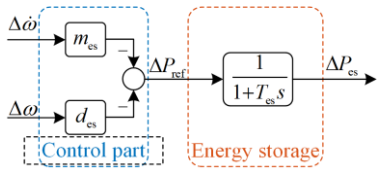

Fig. 1. Frequency response model of energy storage.

The control component obtains the power reference for frequency regulation from the frequency dynamics of the access point. Energy storage generates power, which is injected into the grid according to a power reference. The corresponding transfer function can be expressed as:

$$\Delta p_{\mathrm{es}i}(s) = \frac{-m_{\mathrm{es}i}s - d_{\mathrm{es}i}}{1 + T_{\mathrm{es}i}s}\Delta\omega_i(s) \tag{3}$$

where $p_{\mathrm{es}i}$ is the output power of the energy storage; $m_{\mathrm{es}i}$ and $d_{\mathrm{es}i}$ are the virtual inertia and droop control parameters of the energy storage, respectively; and $T_{\mathrm{es}i}$ is the response time constant of the energy storage.

The response time varies depending on the type of energy storage, which significantly influences the required size of the energy storage [29]. As known, the frequency of the system is closely related to the active power, the larger the unbalanced active power, the greater the frequency deviation. Energy storage with a fast dynamic response (T_{es} is small) absorbs and releases power quickly, which can effectively suppress the rapid fluctuation of active power in the system and

quickly suppress the frequency change of the system. The responses of the output power and energy of different types of energy storage (with different T_{es}) are shown in Fig. 2 under the same control parameters and frequency step disturbances. It can be concluded that energy storage with a smaller T_{es} can provide power and energy more quickly to suppress frequency step changes. However, this also implies that a larger power and energy capacity for energy storage with a smaller T_{es} is necessary. In summary, the types of energy storage, control parameters, and capacities are closely coupled.

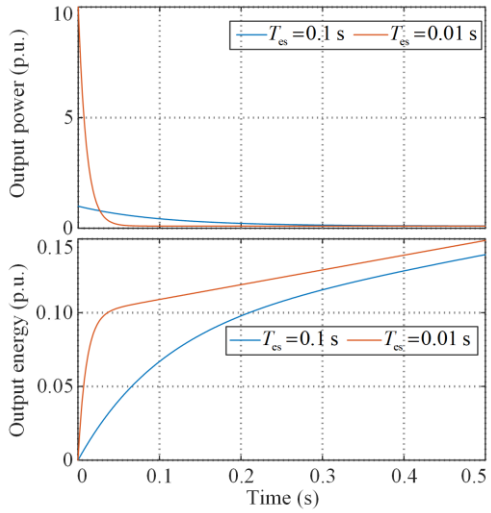

Fig. 2. Step response of different types of energy storage.

This study considers two types of energy storage with different characteristics. The first one is high-rate energy storage, such as in supercapacitors. The response time of this type of energy storage is short, and in general, each cell has a large power capacity and a small energy capacity. The other one is low-rate energy storage such as lithium batteries. The response time of this type of energy storage is long, while the energy capacity of each cell is high but the power capacity is low. The two types of energy storage are denoted by the subscripts 'H' and 'L', respectively. For example, $\Delta p_{\mathrm{esH}i}$ and $\Delta p_{\mathrm{esL}i}$ denote the output power of the high-rate and low-rate energy storage systems, respectively.

C. Frequency Response Model of the Whole System

An AC system with n generators is considered, while high-rate and low-rate energy storage systems are connected near each generator bus.

In this study, renewable energy plants are operated in the maximum power point tracking (MPPT) mode to enhance their efficient utilization of renewable energy. Hence, the renewable energy sources that do not participate in frequency regulation are assumed to be constant power sources. This approach simulates the need for additional frequency regulation resources such as energy storage in high-penetration renewable-energy power systems.

If renewable energy sources are actively engaged in frequency regulation, a similar frequency response model can be established for thermal generators and energy storage. Specifically, renewable energy units that adopt virtual inertia droop control based on grid-following control, whose inertia response has a time delay, can be modeled in a manner similar to energy storage. For grid-forming control, renewable energy units imitating the swing and inertia characteristics of a synchronous generator can be modeled in a manner similar to that of the synchronous generator.

Equation (3) can be rewritten as:

$$\begin{cases} \Delta p_{\mathrm{es}i} = -\dfrac{m_{\mathrm{es}i}}{T_{\mathrm{es}i}}\Delta\omega_i + \Delta\tilde{p}_{\mathrm{es}i} \\ T_{\mathrm{es}i}\Delta\dot{\tilde{p}}_{\mathrm{es}i} = \left(\dfrac{m_{\mathrm{es}i}}{T_{\mathrm{es}i}} - d_{\mathrm{es}i}\right)\Delta\omega_i - \Delta\tilde{p}_{\mathrm{es}i} \end{cases} \tag{4}$$

where $\Delta\tilde{p}_{\mathrm{es}i}$ is the auxiliary state variable.

By combining (1) and (4), the frequency of the generator, including hybrid energy storage system support, can be obtained as follows:

$$\Delta\dot{\omega}_i = -\frac{m_{\mathrm{esH}i}/T_{\mathrm{esH}i} + m_{\mathrm{esL}i}/T_{\mathrm{esL}i} + d_i}{m_i}\Delta\omega_i + \frac{1}{m_i}\Delta p_{\mathrm{m}i} - \frac{1}{m_i}\Delta p_{\mathrm{e}i} + \frac{1}{m_i}\Delta\tilde{p}_{\mathrm{esH}i} + \frac{1}{m_i}\Delta\tilde{p}_{\mathrm{esL}i} + \frac{1}{m_i}\Delta u_i \tag{5}$$

The electromagnetic power fluctuation $\Delta p_{\mathrm{e}i}$ can be derived by the linearized model [30] as:

$$\Delta\dot{p}_{\mathrm{e}i} = \sum_{j=1}^{n} L_{ij}\Delta\omega_j \tag{6}$$

where L_{ij} is the element of the Laplacian matrix $\boldsymbol{L}$ for the grid, and can be expressed as:

$$L_{ij} = \begin{cases} \displaystyle\sum_{k=1}^{n} V_i V_k b_{ik}\cos(\theta_i - \theta_k), & i = j \\ -V_i V_j b_{ij}\cos(\theta_i - \theta_j), & i \neq j \end{cases} \tag{7}$$

where V is the voltage magnitude; b is the line susceptance; and θ is the angle of the generator at the equilibrium power flow. The linearized electromagnetic power fluctuation implicitly makes the following assumptions.

1) Because this study focuses on the role of energy storage in frequency support and the dynamics of voltage control are at a smaller scale than the frequency, the voltage magnitude is assumed to be constant.

2) Lossless lines are approximated for the high-voltage transmission grid.

3) Reactive power flows do not affect frequency.

By combining (2), (4), and (6), the simplified frequency response model of the entire system can be written as follows:

$$\begin{cases} \dot{\boldsymbol{x}} = \boldsymbol{A}\boldsymbol{x} + \boldsymbol{B}\boldsymbol{u} \\ \boldsymbol{y} = \boldsymbol{C}\boldsymbol{x} \end{cases} \tag{8}$$

$$\boldsymbol{x} = \left[\Delta\boldsymbol{\omega} \quad \Delta\boldsymbol{\mu} \quad \Delta\boldsymbol{p}_{\mathrm{HP}} \quad \Delta\boldsymbol{p}_{\mathrm{RH}} \quad \Delta\boldsymbol{p}_{\mathrm{e}} \quad \Delta\tilde{\boldsymbol{p}}_{\mathrm{esH}} \quad \Delta\tilde{\boldsymbol{p}}_{\mathrm{esL}}\right]^{\mathrm{T}} \tag{9}$$

$$\boldsymbol{A} = \begin{bmatrix} -\dfrac{\dfrac{\boldsymbol{m}_{\mathrm{esH}}}{T_{\mathrm{esH}}} + \dfrac{\boldsymbol{m}_{\mathrm{esL}}}{T_{\mathrm{esL}}} + \boldsymbol{d}}{\boldsymbol{m}} & 0 & \dfrac{F_{\mathrm{HP}}}{\boldsymbol{m}} & \dfrac{(1-F_{\mathrm{HP}})}{\boldsymbol{m}} & \dfrac{1}{\boldsymbol{m}} & \dfrac{1}{\boldsymbol{m}} & \dfrac{1}{\boldsymbol{m}} \\ -\dfrac{1}{T_{\mathrm{G}}R} & -\dfrac{1}{T_{\mathrm{G}}} & 0 & 0 & 0 & 0 & 0 \\ 0 & \dfrac{1}{T_{\mathrm{CH}}} & -\dfrac{1}{T_{\mathrm{CH}}} & 0 & 0 & 0 & 0 \\ 0 & 0 & \dfrac{1}{T_{\mathrm{RH}}} & -\dfrac{1}{T_{\mathrm{RH}}} & 0 & 0 & 0 \\ \sum_{j=1}^{n} L_{ij} & 0 & 0 & 0 & 0 & 0 & 0 \\ \left(\dfrac{\boldsymbol{m}_{\mathrm{esH}}}{T_{\mathrm{esH}}^2} - \dfrac{\boldsymbol{d}_{\mathrm{esH}}}{T_{\mathrm{esH}}}\right) & 0 & 0 & 0 & 0 & -\dfrac{1}{T_{\mathrm{esH}}} & 0 \\ \left(\dfrac{\boldsymbol{m}_{\mathrm{esL}}}{T_{\mathrm{esL}}^2} - \dfrac{\boldsymbol{d}_{\mathrm{esL}}}{T_{\mathrm{esL}}}\right) & 0 & 0 & 0 & 0 & -\dfrac{1}{T_{\mathrm{esL}}} & 0 \end{bmatrix} \tag{10}$$

$$\boldsymbol{B} = \left[\boldsymbol{I}/\boldsymbol{m} \quad 0 \quad 0 \quad 0 \quad 0 \quad 0 \quad 0\right]^{\mathrm{T}} \tag{11}$$

$$\boldsymbol{C} = \begin{bmatrix} \boldsymbol{I}_n & 0 & 0 & 0 & 0 & 0 & 0 \\ -\dfrac{\boldsymbol{m}_{\mathrm{esH}}}{T_{\mathrm{esH}}} & 0 & 0 & 0 & 0 & \boldsymbol{I}_n & 0 \\ -\dfrac{\boldsymbol{m}_{\mathrm{esL}}}{T_{\mathrm{esL}}} & 0 & 0 & 0 & 0 & 0 & \boldsymbol{I}_n \end{bmatrix} \tag{12}$$

$$\boldsymbol{y} = \left[\Delta\boldsymbol{\omega} \quad \Delta\boldsymbol{p}_{\mathrm{esH}} \quad \Delta\boldsymbol{p}_{\mathrm{esL}}\right]^{\mathrm{T}} \tag{13}$$

where $\Delta\boldsymbol{\omega}$, $\Delta\boldsymbol{\mu}$, $\Delta\boldsymbol{p}_{\mathrm{HP}}$, $\Delta\boldsymbol{p}_{\mathrm{RH}}$, $\Delta\boldsymbol{p}_{\mathrm{e}}$, $\Delta\tilde{\boldsymbol{p}}_{\mathrm{esH}}$, $\Delta\tilde{\boldsymbol{p}}_{\mathrm{esL}}$, $\Delta\boldsymbol{p}_{\mathrm{esH}}$, and $\Delta\boldsymbol{p}_{\mathrm{esL}}$ are the column vectors of the corresponding variables; while $\boldsymbol{m}$, $\boldsymbol{m}_{\mathrm{esH}}$, $\boldsymbol{m}_{\mathrm{esL}}$, $\boldsymbol{d}$, $\boldsymbol{d}_{\mathrm{esH}}$, and $\boldsymbol{d}_{\mathrm{esL}}$ are the diagonal matrixes consisting of the corresponding variables. The output vector $\boldsymbol{y}$ comprises the frequency and output power of the hybrid energy storage system for each bus, whereas the input vector $\boldsymbol{u}$ is the disturbance vector obtained via Kron reduction [31].

The response of the system to the step disturbance $\boldsymbol{u}$ can be expressed explicitly as:

$$\boldsymbol{y}(t) = \boldsymbol{C}\left(\sum_{i=1}^{7n} \boldsymbol{q}_i \frac{1}{\lambda_i}(\mathrm{e}^{\lambda_i t} - 1)\boldsymbol{w}_i^{\mathrm{T}}\right)\boldsymbol{B}\boldsymbol{u} = \sum_{i=1}^{7n} \boldsymbol{r}_i \frac{1}{\lambda_i}(\mathrm{e}^{\lambda_i t} - 1)\boldsymbol{u} \tag{14}$$

where λ_i is the eigenvalue of $\boldsymbol{A}$; $\boldsymbol{w}_i$ and $\boldsymbol{q}_i$ are the normalized left and right eigenvectors corresponding to λ_i, respectively; the residue $\boldsymbol{r}_i = \boldsymbol{C}\boldsymbol{q}_i\boldsymbol{w}_i^{\mathrm{T}}$; the left eigenvector matrix $\boldsymbol{w} = \left[\boldsymbol{w}_1^{\mathrm{T}} \ \boldsymbol{w}_2^{\mathrm{T}} \cdots \boldsymbol{w}_{7\mathrm{n}}^{\mathrm{T}}\right]^{\mathrm{T}}$; the right eigenvector matrix $\boldsymbol{q} = \left[\boldsymbol{q}_1 \ \boldsymbol{q}_2 \cdots \boldsymbol{q}_{7\mathrm{n}}\right]$; and the relationship between two matrices is $\boldsymbol{w}\boldsymbol{A}\boldsymbol{q} = \boldsymbol{\Lambda} = \mathrm{diag}\left\{\lambda_1, \lambda_2, \cdots, \lambda_{7\mathrm{n}}\right\}$.

III. Hybrid Energy Storage Configuration

This study focuses on the minimum investment demand and distribution of energy storage under power disturbances with frequency security constraints. RoCoF, maximum frequency deviation, and steady-state frequency deviation must satisfy the system constraints during the dynamic process. Although the step response of the simplified system has been expressed explicitly considering the spatial distribution characteristics of frequency, the frequency response model is not linearized, and the relationship between the frequency constraints and the output power of hybrid energy systems cannot be directly established. Hence, in this section, we first propose the calculation of the frequency indices, power capacity, and energy capacity of the hybrid energy storage system. For convenient optimization, a gradient expression of these variables is then proposed that takes into account the energy storage controller parameters.

A. Indices Calculation

1) Rate of Change of Frequency

RoCoF characterizes the system inertia, and a large RoCoF affects the life of the generator, thereby triggering tripping protection. RoCoF is measured at a time interval of 100 ms to 2 s [32]. In this study, we adopt 500 ms after a disturbance as the time interval for RoCoF measures, as in [33]. The step response of frequency can be derived from (14) as follows:

$$\Delta\boldsymbol{\omega}(t) = \boldsymbol{D}_{\omega}\boldsymbol{y}(t) \tag{15}$$

where $\boldsymbol{D}_{\omega} = \left[\boldsymbol{I}_n \ 0 \ 0\right]$.

Substituting t=0.5 s into (15), the RoCoF of all nodes can be obtained as.

$$\boldsymbol{K}_{\mathrm{RF}} = 2\boldsymbol{D}_{\omega}\sum_{i=1}^{7n} \boldsymbol{r}_i \frac{1}{\lambda_i}(\mathrm{e}^{0.5\lambda_i} - 1)\boldsymbol{u} \tag{16}$$

where $\boldsymbol{K}_{\mathrm{RF}} = \left[K_{\mathrm{RF1}} \ K_{\mathrm{RF2}} \ \cdots \ K_{\mathrm{RF}n}\right]^{\mathrm{T}}$, and $K_{\mathrm{RF}i}$ is the RoCoF of generator i.

2) Frequency Nadir

Frequency must remain within the allowable range during the entire dynamic process [23]. The time of the frequency nadir $\boldsymbol{t}_{\mathrm{nadir}}$ can be calculated using the Newton iteration method as.

$$\boldsymbol{t}_{\mathrm{nadir}}(k+1) = \boldsymbol{t}_{\mathrm{nadir}}(k) - \frac{\Delta\dot{\boldsymbol{\omega}}(\boldsymbol{t}_{\mathrm{nadir}}(k))}{\Delta\ddot{\boldsymbol{\omega}}(\boldsymbol{t}_{\mathrm{nadir}}(k))} \tag{17}$$

where $\boldsymbol{t}_{\mathrm{nadir}}(k) = \left[t_{\mathrm{nadir1}}(k) \ t_{\mathrm{nadir2}}(k) \ \cdots \ t_{\mathrm{nadirn}}(k)\right]^{\mathrm{T}}$ denotes the time vector of the frequency nadir for all

generators at the k^{th} iteration step; $\Delta\dot{\boldsymbol{\omega}}$ and $\Delta\ddot{\boldsymbol{\omega}}$ are the first- and second-order derivatives of the frequency respectively, and are expressed as follows:

$$\Delta\dot{\boldsymbol{\omega}}(\boldsymbol{t}_{\text{nadir}}(k)) = \boldsymbol{D}_{\omega}\sum_{i=1}^{7n}\boldsymbol{r}_i \odot \mathrm{e}^{\lambda_i t_{\text{nadir}}(k)}\boldsymbol{u} \tag{18}$$

$$\Delta\ddot{\boldsymbol{\omega}}(\boldsymbol{t}_{\text{nadir}}(k)) = \boldsymbol{D}_{\omega}\sum_{i=1}^{7n}\lambda_i\boldsymbol{r}_i \odot \mathrm{e}^{\lambda_i t_{\text{nadir}}(k)}\boldsymbol{u} \tag{19}$$

where '$\odot$' is the Hadamard product. When the iteration converges $\boldsymbol{t}_{\text{nadir}}(k)\to\boldsymbol{t}_{\text{nadir}}$, the frequency nadir can be obtained as:

$$\Delta\boldsymbol{f}_{\text{nadir}} = \Delta\boldsymbol{\omega}(\boldsymbol{t}_{\text{nadir}})/2\pi \tag{20}$$

where $\Delta\boldsymbol{f}_{\text{nadir}} = \left[\Delta f_{\text{nadir1}}, \Delta f_{\text{nadir1}}\cdots\Delta f_{\text{nadirn}}\right]^{\mathrm{T}}$.

3) Steady-state Frequency

In the frequency recovery process of the secondary frequency control, there will be a frequency deviation for a long time. Although this frequency deviation is not as large as that of the frequency nadir, the process duration is longer. This should be within a certain range. Because the secondary control process is uncertain, the steady-state frequency deviation after primary frequency control is regarded as a frequency safety index. Considering the secondary frequency control process, the actual frequency deviation is smaller than this index, which satisfies the conservation requirement.

The frequency at steady state depends on the damping of the rotor, adjustment factor for the governor, and droop parameters of the energy storage. The expression of steady-state frequency deviation Δf_{ss} is given as:

$$\Delta f_{\text{ss}} = \sum_{i=1}^{n}u_i \Big/ \left(2\pi\sum_{i=1}^{n}d_i + 1/R_i + d_{\text{esH}i} + d_{\text{esL}i}\right) \tag{21}$$

4) Power Capacity of Hybrid Energy Storage

Based on (14), the output power of the hybrid energy storage can be calculated as:

$$\Delta\boldsymbol{p}(t) = \boldsymbol{D}_{\text{p}}\boldsymbol{y}(t) \tag{22}$$

where the output power is denoted as $\Delta\boldsymbol{p} = \left[\Delta\boldsymbol{p}_{\text{esH}}\ \Delta\boldsymbol{p}_{\text{esL}}\right]^{\mathrm{T}}$, and there is:

$$\boldsymbol{D}_{\text{p}} = \begin{bmatrix} 0 & \boldsymbol{I}_n & 0 \\ 0 & 0 & \boldsymbol{I}_n \end{bmatrix} \tag{23}$$

If the power capacity of the energy storage is insufficient to maintain the power demand in (14), the frequency indices deviate from the expected values obtained by (16), (20), and (21), This causes the frequency to exceed the limit. Hence, the power capacity of the hybrid energy storage must be greater than the extreme power response. Similar to (17)–(19), the extremum time $\boldsymbol{t}_{\text{p}}$ of $\Delta\boldsymbol{p}_{\text{esH}}$ and $\Delta\boldsymbol{p}_{\text{esL}}$ can be calculated using the Newton iteration as:

$$\begin{cases} \boldsymbol{t}_{\text{p}}(k+1) = \boldsymbol{t}_{\text{p}}(k) - \dfrac{\Delta\dot{\boldsymbol{p}}(\boldsymbol{t}_{\text{p}}(k))}{\Delta\ddot{\boldsymbol{p}}(\boldsymbol{t}_{\text{p}}(k))} \\ \Delta\dot{\boldsymbol{p}}(\boldsymbol{t}_{\text{p}}(k)) = \boldsymbol{D}_{\text{p}}\sum_{i=1}^{7n}\boldsymbol{r}_i \odot e^{\lambda_i t_{\text{p}}(k)}\boldsymbol{u} \\ \Delta\ddot{\boldsymbol{p}}(\boldsymbol{t}_{\text{p}}(k)) = \boldsymbol{D}_{\text{p}}\sum_{i=1}^{7n}\lambda_i\boldsymbol{r}_i \odot e^{\lambda_i t_{\text{nadir}}(k)}\boldsymbol{u} \end{cases} \tag{24}$$

where $\boldsymbol{t}_{\text{p}} = \left[t_{\text{p1}}\ \ t_{\text{p2}}\cdots\ t_{\text{p}2n}\right]^{\mathrm{T}}$. When the iteration converges $\boldsymbol{t}_{\text{p}}(k)\to\boldsymbol{t}_{\text{p}}$, the extremum of the output power of the hybrid energy storage can be obtained. The power capacity of the energy storage systems should satisfy the following constraints:

$$-\boldsymbol{P}_{\text{es}} \leqslant \Delta\boldsymbol{p}(\boldsymbol{t}_{\text{p}}) \leqslant \boldsymbol{P}_{\text{es}} \tag{25}$$

where $\boldsymbol{P}_{\text{es}} = \left[\boldsymbol{P}_{\text{esH}}\ \ \boldsymbol{P}_{\text{esL}}\right]^{\mathrm{T}}$ denotes the power capacity of the hybrid energy storage system.

5) Energy Capacity of Hybrid Energy Storage

The energy variation of the hybrid energy storage during frequency support can be calculated by integrating (22) as:

$$\Delta\boldsymbol{E}(t) = \int_0^t \Delta\boldsymbol{p}(\tau)\mathrm{d}\tau = \boldsymbol{D}_{\text{p}}\sum_{i=1}^{7n}\boldsymbol{r}_i\left(\frac{1}{\lambda_i^{\,2}}\mathrm{e}^{\lambda_i t} - \frac{1}{\lambda_i}t - \frac{1}{\lambda_i^{\,2}}\right)\boldsymbol{u} \tag{26}$$

The extremum time $\boldsymbol{t}_{\text{e}}$ of energy variation can also be given by the Newton iteration:

$$\begin{cases} \boldsymbol{t}_{\text{e}}(k+1) = \boldsymbol{t}_{\text{e}}(k) - \dfrac{\Delta\dot{\boldsymbol{E}}(\boldsymbol{t}_{\text{e}}(k))}{\Delta\ddot{\boldsymbol{E}}(\boldsymbol{t}_{\text{e}}(k))} \\ \Delta\dot{\boldsymbol{E}}(\boldsymbol{t}_{\text{e}}(k)) = \boldsymbol{D}_{\text{p}}\sum_{i=1}^{7n}\boldsymbol{r}_i \odot \left(\dfrac{1}{\lambda_i}\mathrm{e}^{\lambda_i t_{\text{e}}(k)} - \dfrac{1}{\lambda_i}\right)\boldsymbol{u} \\ \Delta\ddot{\boldsymbol{E}}(\boldsymbol{t}_{\text{e}}(k)) = \boldsymbol{D}_{\text{p}}\sum_{i=1}^{7n}\boldsymbol{r}_i \odot \mathrm{e}^{\lambda_i t_{\text{e}}(k)}\boldsymbol{u} \end{cases} \tag{27}$$

where $\boldsymbol{t}_{\text{e}} = \left[t_{\text{e1}}\ \ t_{\text{e2}}\cdots\ t_{\text{e}2n}\right]^{\mathrm{T}}$. The energy capacity of the energy storage systems must satisfy the following constraints:

$$-\boldsymbol{E}_{\text{es}} \leqslant \Delta\boldsymbol{E}(\boldsymbol{t}_{\text{e}}) \leqslant \boldsymbol{E}_{\text{es}} \tag{28}$$

where $\boldsymbol{E}_{\text{es}} = \left[\boldsymbol{E}_{\text{esH}}\ \boldsymbol{E}_{\text{esL}}\right]^{\mathrm{T}}$ denotes the energy capacity of the hybrid energy storage system.

B. Optimal Placement of Hybrid Energy Storage

We focus on the optimal placement of energy storage systems to minimize the investment in energy storage, subject to the constraints of the frequency indices. The calculation method for the frequency metrics and hybrid energy storage capacity has been presented in Section III.A. However, these metrics are calculated using eigenvalues and eigenvectors, and there is no explicit relationship between the frequency indices and the configuring energy storage systems. The eigenvalues

and corresponding eigenvectors of the system are associated with the controller parameters of the energy storage systems. Therefore, the controller parameters are adopted as optimization variables κ in this paper. The original energy storage optimal placement and capacity problem is formulated as an optimal control parameter problem for energy storage systems to ensure sufficient frequency support. The optimization problem can be summarized as follows:

$$\min_{\kappa} \ \boldsymbol{1}_{\mathrm{n}}^{\mathrm{T}}(C_{\mathrm{ph}}\boldsymbol{P}_{\mathrm{esH}}+C_{\mathrm{pl}}\boldsymbol{P}_{\mathrm{esL}}+C_{\mathrm{eh}}\boldsymbol{E}_{\mathrm{esH}}+C_{\mathrm{el}}\boldsymbol{E}_{\mathrm{esL}}) \quad (29)$$

s.t. (25), (28), and

$$-\boldsymbol{1}_{\mathrm{n}}K_{\mathrm{RF\,max}} \leqslant \boldsymbol{K}_{\mathrm{RF}} \leqslant \boldsymbol{1}_{\mathrm{n}}K_{\mathrm{RF\,max}} \quad (30)$$

$$-\boldsymbol{1}_{\mathrm{n}}\Delta f_{\mathrm{nadir,max}} \leqslant \Delta \boldsymbol{f}_{\mathrm{nadir}} \leqslant \boldsymbol{1}_{\mathrm{n}}\Delta f_{\mathrm{nadir,max}} \quad (31)$$

$$-\Delta f_{\mathrm{ss,max}} \leqslant \Delta f_{\mathrm{ss}} \leqslant \Delta f_{\mathrm{ss,max}} \quad (32)$$

where $\kappa=(\boldsymbol{m}_{\mathrm{esH}},\boldsymbol{m}_{\mathrm{esL}},\boldsymbol{d}_{\mathrm{esL}})$ denotes the optimization variables; $\boldsymbol{1}_{\mathrm{n}}$ is an n-dimensional column vector with all elements of 1; C_{ph} and C_{pl} are the costs per unit power of the high-rate energy storage and the low-rate energy storage, respectively; C_{eh} and C_{el} are the costs per unit energy of the high-rate energy storage and the low-rate energy storage, respectively; $K_{\mathrm{RF\,max}}$, $\Delta f_{\mathrm{nadir,max}}$, and $\Delta f_{\mathrm{ss,max}}$ are the maximum allowable RoCoF, the maximum allowable frequency deviation, and the maximum allowable steady-state frequency deviation, respectively.

This study focuses on the frequency security constraints during inertia and primary frequency control processes following power disturbances. After a disturbance, the power flow undergoes dynamic changes. However, owing to the short duration of the studied frequency control dynamics and its exclusive reliance on local frequency monitoring, it does not ensure power flow constraints on the transmission lines. The assurance of power-flow constraints on lines necessitates coordinated secondary and tertiary frequency control mechanisms among the generating units, which is beyond the scope of this study. Hence, the power-flow constraint is not included in this study.

Remark 1: The configuration results provide the minimum investment in hybrid energy storage to provide sufficient frequency support demanded by the power system. The configuration scheme includes the power capacity, energy capacity, and placement of hybrid energy storage systems considering spatial differences in the frequency response. Therefore, it not only provides the minimum investment for ensuring frequency stability of a system but also identifies boundary conditions for the scheduling of energy storage systems. In other words, when the system is scheduled, the power and energy capacities should be reserved for energy storage systems in different locations to ensure the stability of the system frequency.

Remark 2: The configuration results also include the energy storage system control parameters. Various energy storage systems possess distinct control parameters. The allocation of the power-supporting frequency is actively adjusted based on the controller coefficients to ensure optimal utilization of power and energy capacity for each storage unit.

C. Gradient Calculation

From (29)–(32), the lack of direct correlation between the controller coefficients and indices makes it difficult to determine the optimum value. Moreover, the expressions for the frequency indices and energy storage capacity are nonlinear. Inspired by [20], the explicit gradient accelerates most numerical optimization computational methods. Hence, it is necessary to assess the explicit gradients of these indices for the control parameters m_{esi} and d_{esi}.

The gradient of the eigenvalues concerning the control parameters can be calculated as:

$$\nabla\lambda_i = \boldsymbol{w}_i^{\mathrm{T}}(\nabla\boldsymbol{A})\boldsymbol{q}_i \quad (33)$$

where

$$\nabla = \frac{\partial}{\partial \boldsymbol{m}_{\mathrm{esH}}}\boldsymbol{m}_{\mathrm{esH}} + \frac{\partial}{\partial \boldsymbol{d}_{\mathrm{esH}}}\boldsymbol{d}_{\mathrm{esH}} + \frac{\partial}{\partial \boldsymbol{m}_{\mathrm{esL}}}\boldsymbol{m}_{\mathrm{esL}} + \frac{\partial}{\partial \boldsymbol{d}_{\mathrm{esL}}}\boldsymbol{d}_{\mathrm{esL}} \quad (34)$$

The gradient of the product of the left and right eigenvectors [34] is given by:

$$\nabla(\boldsymbol{q}_i\boldsymbol{w}_i^{\mathrm{T}}) = \sum_{j=1,j\neq i}^{n}\boldsymbol{q}_j\nabla c_{ij}\boldsymbol{w}_i^{\mathrm{T}} - \boldsymbol{q}_i\nabla c_{ji}\boldsymbol{w}_j^{\mathrm{T}} \quad (35)$$

where

$$\nabla c_{ij} = \frac{\boldsymbol{w}_j^{\mathrm{T}}\nabla\boldsymbol{A}\boldsymbol{q}_i^{\mathrm{T}}}{\lambda_i-\lambda_j} \quad (36)$$

By combining the definition of residue r_i and (35), the gradient of the residue can be derived as:

$$\nabla\boldsymbol{r}_i = \nabla\boldsymbol{C}\boldsymbol{q}_i\boldsymbol{w}_i^{\mathrm{T}}\boldsymbol{B} + \boldsymbol{C}\nabla(\boldsymbol{q}_i\boldsymbol{w}_i^{\mathrm{T}})\boldsymbol{B} + \boldsymbol{C}\boldsymbol{q}_i\boldsymbol{w}_i^{\mathrm{T}}\nabla\boldsymbol{B} \quad (37)$$

Based on (33) and (37), the RoCoF gradient can be determined as:

$$\nabla\boldsymbol{K}_{\mathrm{RF}} = 2\boldsymbol{D}_{\omega}\sum_{i=1}^{7n}\left[\nabla\frac{\boldsymbol{r}_i}{\lambda_i}(\mathrm{e}^{0.5\lambda_i}-1)+0.5\frac{\boldsymbol{r}_i}{\lambda_i}\nabla\lambda_i\mathrm{e}^{0.5\lambda_i}\right]\boldsymbol{u} \quad (38)$$

The expressions of $\Delta\boldsymbol{f}_{\mathrm{nadir}}$, $\Delta\boldsymbol{p}(\boldsymbol{t}_{\mathrm{p}})$, and $\Delta\boldsymbol{E}(\boldsymbol{t}_{\mathrm{e}})$ are related to $\boldsymbol{t}_{\mathrm{nadir}}$, $\boldsymbol{t}_{\mathrm{p}}$, and $\boldsymbol{t}_{\mathrm{e}}$, respectively. Because it is impossible to obtain an explicit expression of these peak times, the gradients of these peak times cannot be obtained. Based on Newton's update in (17), we can approximate the gradient of the peak time as:

$$\nabla\boldsymbol{t}_{\mathrm{nadir}} = -\left.\frac{\nabla(\Delta\dot{\boldsymbol{\omega}})\odot\Delta\ddot{\boldsymbol{\omega}}-\Delta\dot{\boldsymbol{\omega}}\odot\nabla(\Delta\ddot{\boldsymbol{\omega}})}{\Delta\ddot{\boldsymbol{\omega}}\odot\Delta\ddot{\boldsymbol{\omega}}}\right|_{\boldsymbol{t}=\boldsymbol{t}_{\mathrm{nadir}}} \quad (39)$$

where the gradient of the derivative of the frequency can be expressed as:

$$\nabla(\Delta\dot{\boldsymbol{\omega}}) = \boldsymbol{D}_{\omega}\sum_{i=1}^{7n}(\nabla\boldsymbol{r}_i + \boldsymbol{r}_i\odot\boldsymbol{t}_{\mathrm{nadir}}\nabla\lambda_i)\odot\mathrm{e}^{\lambda_i\boldsymbol{t}_{\mathrm{nadir}}}\boldsymbol{u} \quad (40)$$

$$\nabla(\Delta\ddot{\boldsymbol{\omega}}) = \boldsymbol{D}_{\omega}\sum_{i=1}^{7n}\begin{pmatrix}\lambda_i\nabla\boldsymbol{r}_i + \boldsymbol{r}_i\nabla\lambda_i + \\ \lambda_i\boldsymbol{r}_i \odot \boldsymbol{t}_{\text{nadir}}\nabla\lambda_i\end{pmatrix}\odot \mathrm{e}^{\lambda_i \boldsymbol{t}_{\text{nadir}}}\boldsymbol{u} \quad (41)$$

The gradients of the other peak times, $\boldsymbol{t}_{\text{p}}$ and $\boldsymbol{t}_{\text{e}}$, are calculated similarly. The gradients of $\Delta\boldsymbol{f}_{\text{nadir}}$, $\Delta\boldsymbol{p}(\boldsymbol{t}_{\text{p}})$, and $\Delta\boldsymbol{E}(\boldsymbol{t}_{\text{e}})$ can be written as follows:

$$\nabla(\Delta\boldsymbol{f}_{\text{nadir}}) = \sum_{i=1}^{7n}\boldsymbol{D}_{\omega}\nabla\frac{\boldsymbol{r}_i}{2\pi\lambda_i}\odot(e^{\lambda_i\boldsymbol{t}_{\text{nadir}}}-1)\boldsymbol{u} + \sum_{i=1}^{7n}\boldsymbol{D}_{\omega}\frac{\boldsymbol{r}_i}{2\pi\lambda_i}\odot(\nabla\lambda_i\boldsymbol{t}_{\text{nadir}} + \lambda_i\nabla\boldsymbol{t}_{\text{nadir}})\odot e^{\lambda_i\boldsymbol{t}_{\text{nadir}}}\boldsymbol{u} \quad (42)$$

$$\nabla(\Delta\boldsymbol{p}(\boldsymbol{t}_{\text{p}})) = \boldsymbol{D}_{\text{p}}\sum_{i=1}^{7n}\boldsymbol{u}\left[\begin{array}{l}\nabla\dfrac{\boldsymbol{r}_i}{\lambda_i}\odot\left(\mathrm{e}^{\lambda_i\boldsymbol{t}_{\text{p}}}-1\right)+ \\ \dfrac{\boldsymbol{r}_i}{\lambda_i}\odot(\nabla\lambda_i\boldsymbol{t}_{\text{p}} + \lambda_i\nabla\boldsymbol{t}_{\text{p}})\odot\mathrm{e}^{\lambda_i\boldsymbol{t}_{\text{p}}}\end{array}\right] \quad (43)$$

$$\nabla(\Delta\boldsymbol{E}(\boldsymbol{t}_{\text{e}})) = \boldsymbol{D}_{\text{p}}\sum_{i=1}^{7n}\left[\nabla\frac{\boldsymbol{r}_i}{\lambda_i^2}\odot(\mathrm{e}^{\lambda_i\boldsymbol{t}_{\text{e}}}-1)\right]\boldsymbol{u} + \boldsymbol{D}_{\text{p}}\sum_{i=1}^{7n}\left[\frac{\boldsymbol{r}_i}{\lambda_i^2}\odot(\nabla\lambda_i\boldsymbol{t}_{\text{e}} + \lambda_i\nabla\boldsymbol{t}_{\text{e}})\odot\mathrm{e}^{\lambda_i\boldsymbol{t}_{\text{e}}}\right]\boldsymbol{u} - \boldsymbol{D}_{\text{p}}\sum_{i=1}^{7n}\left[\nabla\frac{\boldsymbol{r}_i}{\lambda_i}\odot\boldsymbol{t}_{\text{e}} + \frac{\boldsymbol{r}_i}{\lambda_i}\odot\nabla\boldsymbol{t}_{\text{e}}\right]\boldsymbol{u} \quad (44)$$

Based on (38) and (42)–(44), problems (29)–(32) can be solved using commercial off-the-shelf nonlinear solvers such as interior point optimizer (IPOPT).

IV. Case Study

In this section, the proposed optimal method for the parameters and placement of hybrid energy storage systems is evaluated using two test systems. A simple two-area power system is adopted in Section IV.C, whereas a large-scale south-east Australian system is adopted in Section IV D.

A. Two-area Power System Case Setup

The two-area system is implemented in Matlab/Simulink to validate the effectiveness of the proposed optimal allocation method. The line diagram of the system is shown in Fig. 3. The simulation of the synchronous generator adopted a sixth-order model with a governor and excitation system, and the parameters are obtained from the classic Kundur two-area system [36]. The total power generation of the system is 2817.25 MW, of which the power generation of wind farm 1 is 667.25 MW.

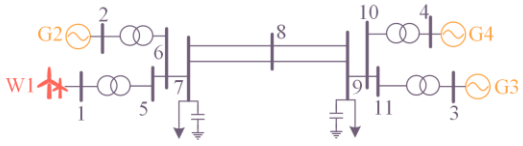

Fig. 3. The single-line diagram of a two-area power system.

The high-power-density energy storage and high-energy-density energy storage in this case are supercapacitors and lithium batteries, respectively. The technical and economic parameters are presented in Table I.

TABLE I
Technical and Economical Parameters

Parameters	Value
Rated frequency (Hz)	50
$K_{\text{RF max}}$ (Hz/s)	0.5
$\Delta f_{\text{nadir,max}}$ (Hz)	0.8
$\Delta f_{\text{ss,max}}$ (Hz)	0.4
C_{ph} ($/kW)	100
C_{pl} ($/kW)	600
C_{eh} ($/kWh)	2000
C_{el} ($/kWh)	100
T_{esh} (s)	0.01
T_{esl} (s)	0.1
T_{f} (min)	15

The optimal energy storage configuration will improve frequency stability during an outage of wind farm 1. To analyze the influence of different application scenarios on the hybrid energy storage configuration results, two typical application scenarios are established in this section, i.e., optimal configurations of energy storage systems with virtual inertia control and virtual inertia droop control, respectively. The former scenario aims to improve the inertia response of the frequency to avoid excessive RoCoF and frequency deviations, whereas the latter also improves the steady-state frequency deviation.

Figure 4 shows the frequency dynamics under an outage of wind farm 1 when there is no energy storage in the system. The maximum RoCoF of different nodes are –1.39 Hz/s, –1.30 Hz/s, and –1.36 Hz/s, respectively. The minimum frequencies of the different nodes are 48.61 Hz, 48.88 Hz, and 48.95 Hz, respectively. The steady-state frequency of the system is 49.57 Hz.

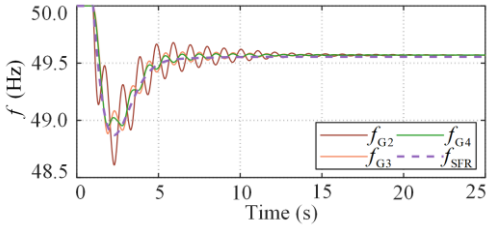

Fig. 4. Frequency dynamics without energy storage.

As shown in Fig. 4, because the disturbance is near generator 2, the frequency drop rate of generator 2 is significantly higher than those of the other units, and its minimum frequency is also lower than those of the other units. The dynamic frequency response in a two-area power system has significant space-time distribution features.

According to the conventional system frequency response (SFR) model [18], the minimum frequency is 48.87 Hz. Compared with the detailed simulation model, the frequency response of the conventional SFR model overestimates the lowest frequency, resulting in a lack

of conservatism in the conventional energy storage optimal configuration.

B. Optimal Placement of Virtual Inertia Control

In this case, the objective of the optimal placement is to minimize the cost of the investment in the hybrid energy storage systems with virtual inertia control, satisfying the RoCoF and frequency deviation constraints. The hybrid energy storage configuration scheme with the proposed method is listed in Table II. Because inertia support requires high power capacity without the need for excessive energy capacity, high-rate energy storage is more cost-effective for inertia support. Hence, Table II shows that only high-rate energy storage is configured. In addition, because the disturbance is located near bus 2, and the interconnection between this region and the region of bus 3 and 4 is weak, all the energy storage is configured at bus 2 in Table II. The configuration scheme demonstrates that the proposed configuration results for this case are reasonable.

TABLE II
HYBRID ENERGY STORAGE CONFIGURATION WITH THE PROPOSED METHOD

Node	2	3	4
m_{esh}	518.2	0	0
m_{esl}	0	0	0
P_{esh} (MW)	542.6	0	0
E_{esh} (MWh)	0.23	0	0
P_{esl} (MW)	0	0	0
E_{esl} (MWh)	0	0	0
Cost ($)	5.47×10^7	0	0

The frequency dynamics after configuring the energy storage based on the proposed scheme are illustrated in Fig. 5. A frequency indicator comparison before and after the energy storage configuration using the proposed method is presented in Table III. From the time-domain simulation results, it can be concluded that the frequency response satisfies the dynamic constraint. Meanwhile, the frequency nadir is very close to the constraint (–0.8 Hz), demonstrating the accuracy of the frequency response model adopted in the proposed method. As a result, the proposed method can consider the space-time distribution features of the frequency response and optimize the control parameters, capacity, and location of the hybrid energy storage, satisfying the frequency dynamic constraints.

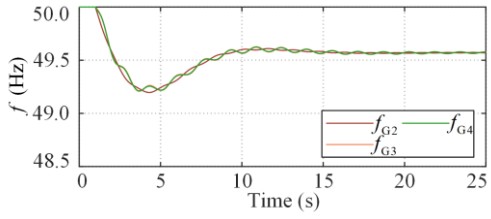

Fig. 5. Frequency dynamics after configuring energy storage with the proposed method.

TABLE III
COMPARISON BEFORE AND AFTER ENERGY STORAGE CONFIGURATION

Indicators	Without energy storage	With the proposed method
K_{RF2} (Hz/s)	–1.39	–0.48
K_{RF3} (Hz/s)	–1.30	–0.31
K_{RF4} (Hz/s)	–1.36	–0.31
Δf_{nadir2} (Hz)	–1.39	–0.80
Δf_{nadir3} (Hz)	–1.12	–0.79
Δf_{nadir4} (Hz)	–1.05	–0.79

To demonstrate the advantage of the proposed method, the energy storage configuration method proposed in [18], in which the frequency of the SFR model is constrained, is used for comparison. The capacity of energy storage required to be configured is 497.6 MW. Because the storage configuration based on the SFR model cannot configure the location and type of storage, a high-rate storage of this capacity is placed in different locations. The simulation results are presented in Fig. 6. It can be observed from Fig. 6(a) that the frequency nadir of the SFR model reaches 49.21 Hz, meeting the system requirements. However, because of the influence of the grid structure, the actual frequency cannot be guaranteed to satisfy the stability requirements. Moreover, when the inertia support energy storage is placed at different locations, the difference in the frequency response is significant. When the energy storage is configured at bus 2 with low inertia and close to the disturbance (consistent with the proposed method), the frequency performance is similar to that shown in Fig. 5. However, because the response speed is ignored, the inertia support of the energy storage is overestimated. The frequency nadir is slightly smaller than the frequency nadir constraint. When the energy storage is configured far away from the disturbance and low-inertia node, both the RoCoF and frequency nadir of generator 2 exceed the limits, while the frequency oscillation of generator 2 is more serious. The comparison illustrates that a suitable position of the inertia support energy storage will also influence the frequency response, and such impact cannot be neglected.

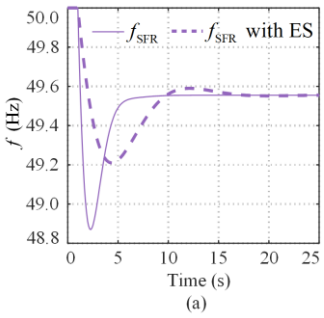

(a)

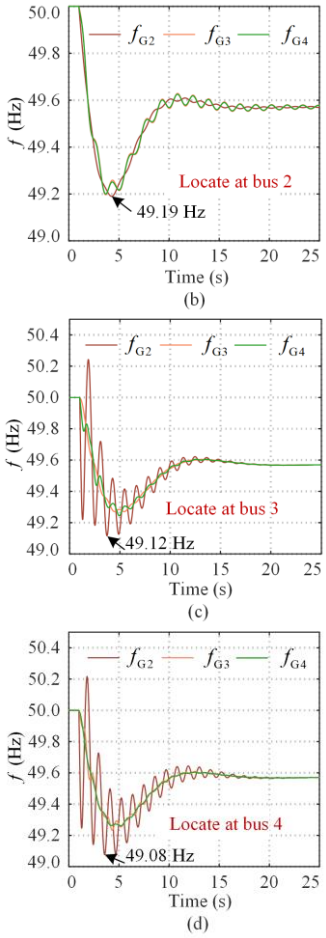

Fig. 6. Frequency dynamics after configuring energy storage with the method in [18]. (a) SFR model. (b) Detailed model with energy storage at bus 2. (c) Detailed model with energy storage at bus 3. (d) Detailed model with energy storage at bus 4.

To further highlight the advantages of the proposed method, the frequency dynamics after configuring energy storage systems using the method in [23] are depicted in Fig. 7. As seen, although the frequency dynamics are improved, the frequency response does not satisfy the frequency nadir constraint. Because the method establishes a linear relationship between the frequency index and inertia coefficient of each node, the interaction between nodes is ignored. As expected, an adequate frequency response cannot be obtained.

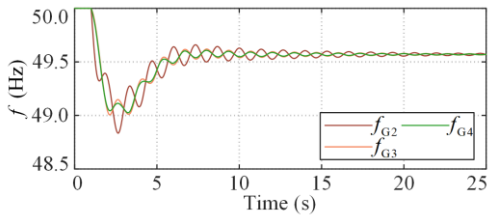

Fig. 7. Frequency dynamics after configuring energy storage with the method in [23].

To illustrate that the proposed method can effectively reduce the computational effort and improve the solution efficiency, the proposed method is compared with a method without a specific gradient. To demonstrate the generality of the conclusions, iterative calculations are performed using 50 initial points. The average calculation efficiencies of the two methods are presented in Table IV, where it can be observed that the minimum values of the objective functions are the same. However, both the number of objective function calculation and the iterative computation time of the proposed method are better than those of the conventional method. The results demonstrate that the proposed optimal method performs better in improving computing efficiency.

TABLE IV
COMPARISON OF AVERAGE COMPUTATIONAL EFFICIENCY

Indicators	Without specific gradient	With the proposed method
Number of function calculations	400	127
Calculation time (s)	62.42	29.23
Best cost ($)	5.47×10^7	5.47×10^7

C. Optimal Placement of Virtual Inertia and Droop Control

Because the steady-state frequency of the system is only 49.57 Hz in Fig. 4, the system requires droop control support in addition to inertia support. Hybrid, high-rate, and low-rate energy storage configuration schemes using the proposed method are listed in Table V. In all the schemes, the energy storage is configured at bus 2.

TABLE V
COMPARISON OF DIFFERENT ENERGY STORAGE CONFIGURATION SCHEMES

Method	Hybrid energy storage	Only high-rate energy storage	Only low-rate energy storage
m_{esh2}	430.67	477.38	0
d_{esh2}	0.34	84.06	0
m_{esl2}	60.34	0	531.65
d_{esl2}	83.72	0	84.06
P_{esh2} (MW)	521.35	537.96	0
E_{esh2} (MWh)	0.16	16.97	0
P_{esL2} (MW)	119.19	0	531.7
E_{esl2} (MWh)	16.8	0	16.97
Cost ($)	7.80×10^7	8.77×10^7	10.8×10^7

As can be seen from Table V, compared to the single energy storage configuration scheme, the cost of the hybrid energy storage configuration scheme is the lowest. Most of the power demand is covered by high-rate energy storage, whereas most of the energy demand is covered by low-rate energy storage. This allocation makes full use of the ratios of the different energy storage systems. Hence, the proposed configuration scheme is more adequate. The sum of the inertia coefficients for different configuration schemes vary because of the different response speeds of the energy

storage. However, because the droop parameter of the energy storage is mainly designed to satisfy the $\Delta f_{ss,max}$ constraint, the sum of the droop coefficients is the same for different energy storage configuration schemes.

The frequency and output power responses of the energy storage with the proposed configuration scheme are shown in Figs. 8 and 9, respectively. The steady-state frequency of the system is recovered to 49.60 Hz, satisfying the $\Delta f_{ss,max}$ constraint. The minimum frequency of 49.29 Hz and the maximum RoCoF of 0.50 Hz/s, are all within the frequency constraints. Based on the power response of the energy storage, the high-rate energy storage mainly provides short-term inertia support, whereas the low-rate energy storage provides long-term droop support. The two types of energy storage cooperate to fully use their respective advantages in terms of power and energy capacities to achieve frequency improvement.

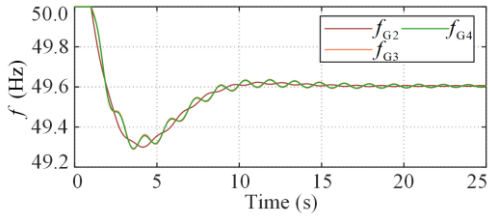

Fig. 8. Frequency response of the proposed virtual inertia and droop control configuration method.

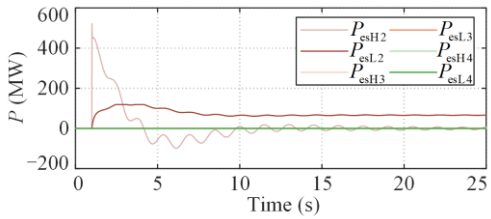

Fig. 9. Power response of the configured hybrid energy storage system.

D. Southeast Australian Power System

To illustrate the applicability of the proposed algorithm in a large real system under different disturbance scenarios, a modified case based on the south-east Australian system in [35] is adopted. The modified line diagram is shown in Fig. 10. The system consists of five areas. Owing to the string topology, the coupling between the areas is very weak. The original nine generators are replaced with wind farms injecting the same power to simulate a power system with high penetration of renewable energy sources. The energy storage configuration target of this case is for the system frequency to be within the constraints when one of the wind farms is disconnected. Hence, there are nine disturbance scenarios in this case.

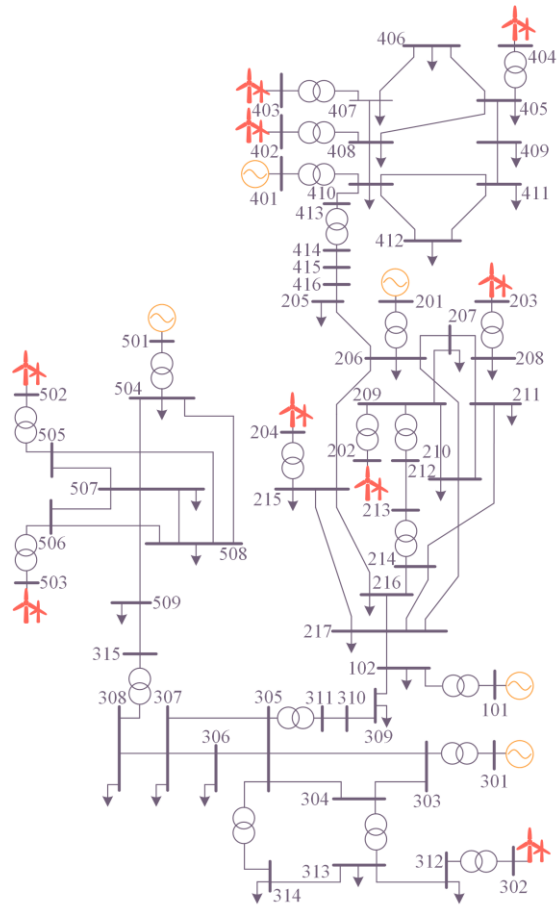

Fig. 10. The single-line diagram of the modified southeast Australian power system.

The hybrid energy storage configuration results obtained using the proposed method are shown in Figs. 11–13. The power demand during the inertia support process is primarily satisfied by the high-rate energy storage systems, while the energy demand during the droop support process is primarily satisfied by the low-rate energy storage. Owing to the limitation of the inertia coefficient for the energy storage in each area, the low-rate energy storage system in area 2 still provides large inertia support. Δf_{nadir} and K_{RF} under the nine disturbance scenarios after configuring hybrid energy storage with the proposed method are shown in Figs. 14 and 15, respectively. As shown in the histograms, the frequency of each area is within the constraint under different disturbances. The simulation results suggest that the proposed method can be adapted to the hybrid energy storage configuration of a large power system under multiple disturbances.

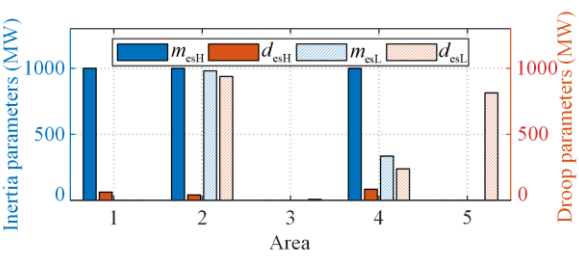

Fig. 11. Optimal inertia and droop coefficient allocations.

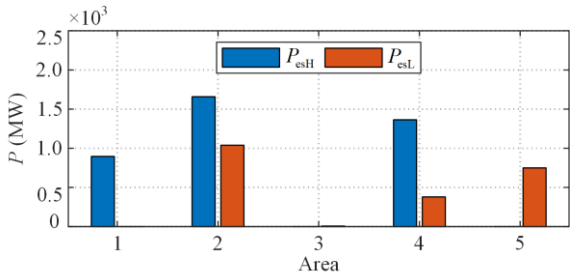

Fig. 12. Optimal power capacity of hybrid energy storage systems.

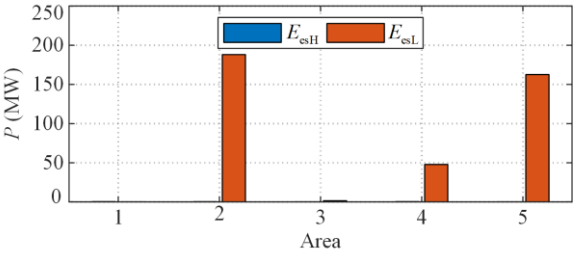

Fig. 13. Optimal energy capacity of hybrid energy storage systems.

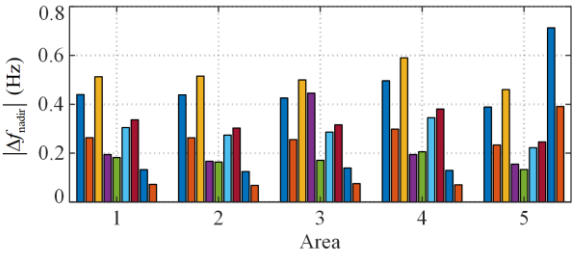

Fig. 14. Maximum frequency deviation under nine disturbance scenarios after configuring hybrid energy storage.

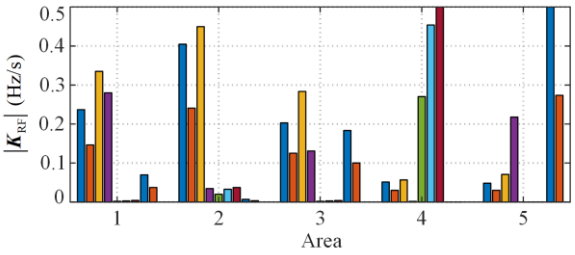

Fig. 15. RoCoF under nine disturbance scenarios after configuring hybrid energy storage.

V. Conclusion

In this study, the problem of placing hybrid energy storage to improve frequency dynamic stability is addressed by considering the spatial distribution characteristics of the frequency response. A simplified frequency response model is developed that considers the dynamic differences between different nodes. A hybrid energy storage configuration model that considers the frequency dynamic constraints at each node is also proposed. This model combines the advantages of high- and low-rate energy storage to satisfy power and energy requirements during frequency support. This reduces investments in energy storage. Moreover, an explicit gradient-method-based hybrid energy storage optimization approach is proposed to improve computational efficiency. The proposed configuration method is validated using a two-area power system and the south-east Australian power system. Time-domain simulation results show that the proposed method is more efficient than the conventional configuration method [23]. A comparison test of the computational efficiency demonstrates that the proposed explicit gradient-based method can significantly improve solution efficiency.

The dynamic frequency variation process can be chronologically divided into three phases: inertia response, primary frequency response, and secondary frequency response. This study primarily addresses the inertia response and primary frequency response following system disturbances, while a secondary frequency control process involving energy storage requirements has not been explored. Future research on enhancing frequency stability with energy storage will incorporate the secondary frequency control aspect to ensure that the constraints on line power flows are satisfied.

Acknowledgment

Not applicable.

Authors' Contributions

Dan Liu: conceptualization, methodology, formal analysis, and writing original draft. Qiufan Yang: validation, investigation, and data curation. Yin Chen: supervision and visualization. Xia Chen: writing- reviewing and editing. Jinyu Wen: funding acquisition, writing-reviewing and editing. All authors read and approved the final manuscript.

Funding

This work is supported by the National Key Research and Development Program (No. 2023YFB2406600), and the National Natural Science Foundation of China (No. U22A6007 and No. 52222703).

Availability of Data and Materials

Please contact the corresponding author for data material request.

Declarations

Competing interests: The authors declare that they have no known competing financial interests or personal relationships that could have appeared to influence the work reported in this article.

Authors' Information

Dan Liu received the master's degree from Chinese Academy of Sciences, Beijing, China, in 2013. She is currently working toward her Ph.D. degree in electrical engineering at Huazhong University of Science and

Technology, Wuhan, China. Her research interests include renewable energy, power storage systems, microgrids, and distributed networks.

Qiufan Yang received the B.S. degree in electrical engineering from Huazhong University of Science and Technology (HUST), Wuhan, China, in 2019. He is currently working toward his Ph.D. degree in electrical engineering at HUST, Wuhan, China. His current research interests include DC microgrids, distributed control, and energy storage technologies.

Yin Chen received the B.S. degree in electrical engineering from the Huazhong University of Science and Technology, Wuhan, China, in 2009, the M.S. degree in electrical engineering from Zhejiang University, Hangzhou, China, in 2014, and the Ph.D. degree in electrical engineering from the University of Strathclyde, Glasgow, UK, in 2020. He is currently a associate researcher with the University of Strathclyde. His research interests include the modeling of power electronic converters, grid integration of renewable power, and stability analysis of the HVDC transmission systems.

Xia Chen received the B.S. degree in power system and its automaton from Wuhan University of Technology, China, in 2006, and the M.S. and Ph.D. degrees in electrical engineering from Huazhong University of Science and Technology (HUST), China, in 2008 and 2012, respectively. She was a post-doctoral research fellow with the University of Hong Kong, from 2012 to 2015. In 2015 she joined the HUST and now she is a professor with the School of Electrical and Electronic Engineering, HUST. Her research interests include energy storage control and operation, renewable energy integration technologies, and new smart grid device.

Jinyu Wen received the B.Eng. and Ph.D. degrees in electrical engineering from Huazhong University of Science and Technology (HUST), Wuhan, China, in 1992 and 1998, respectively. He was a visiting student from 1996 to 1997 and research fellow from 2002 to 2003 at the University of Liverpool, UK, and a senior visiting researcher at the University of Texas at Arlington, USA in 2010. From 1998 to 2002 he was a director engineer in XJ Electric Co. Ltd. in China. In 2003 he joined the HUST and now is a professor at HUST. His current research interests include renewable energy integration, energy storage application, DC grid, and power system operation and control.

REFERENCES

[1] Y. Chen, S. M. Mazhari, and C. Y. Chung *et al.*, "Rotor angle stability prediction of power systems with high wind power penetration using a stability index vector," *IEEE Transactions on Power Systems*, vol. 35, no. 6, pp. 4632-4643, Nov. 2020.

[2] D. Ortiz-Villalba, C. Rahmann, and R. Alvarez *et al.*, "Practical framework for frequency stability studies in power systems with renewable energy sources," *IEEE Access*, vol. 8, pp. 202286-202297, Nov. 2020.

[3] L. Badesa, F. Teng, and G. Strbac, "Conditions for regional frequency stability in power system scheduling—part I: theory," *IEEE Transactions on Power System*, vol. 36, no. 6, pp. 5558-5566, Nov. 2021.

[4] L. Badesa, F. Teng, and G. Strbac, "Conditions for regional frequency stability in power system scheduling—part II: application to unit commitment," *IEEE Transactions on Power Systems*, vol. 36, no. 6, pp. 5567-5577, Nov. 2021.

[5] X. Zhao, H. Wei, and J. Qi *et al.*, "Frequency stability constrained optimal power flow incorporating differential algebraic equations of governor dynamics," *IEEE Transactions on Power System*, vol. 36, no. 3, pp. 1666-1676, May 2021.

[6] E. Alves, G. Bergna-Diaz, and D. Brandao *et al.*, "Sufficient conditions for robust frequency stability of a AC power systems," *IEEE Transactions on Power Systems*, vol. 36, no. 3, pp. 2684-2692, May 2021.

[7] N. Nguyen, S. Almasabi, and A. Bera *et al.*, "Optimal power flow incorporating frequency security constraint," *IEEE Transactions on Industry Applications*, vol. 55, no. 6, pp. 6508-6516, Sept. 2019.

[8] X. Li , Z. Wang, and Y. Chen *et al.*, "Active frequency support strategy for new energy inverters based on virtual inertia fuzzy adaptive control," *Power System Protection and Control*, vol. 52, no. 20, pp. 25-37, Oct. 2024. (in Chinese)

[9] Y. Zeng, Q. Yang, and Y. Lin *et al*., "Fractional-order virtual inertia control and parameter tuning for energy-storage system in low-inertia power grid," *Protection and Control of Modern Power Systems*, vol. 9, no. 5, pp. 70-83, Sept. 2024.

[10] J. Dave, H. Ergun, and D. Van Hertem, "Incorporating dc grid protection, frequency stability and reliability into offshore DC grid planning," *IEEE Transactions on Power Delivery*, vol. 35, no. 6, pp. 2772-2781, Dec. 2020.

[11] M. Esmaili, M. Ghamsari-Yazdel, and N. Amjady *et al.*, "Convex model for controlled islanding in transmission expansion planning to improve frequency stability," *IEEE Transactions on Power Systems*, vol. 36, no. 1, pp. 58-67, Jan. 2021.

[12] H. García-Pereira, M. Blanco, and G. Martínez-Lucas *et al.*, "Comparison and influence of flywheels energy storage system control schemes in the frequency regulation of isolated power systems," *IEEE Access*, vol. 10, pp. 37892-37911, Mar. 2022.

[13] Y. Yuan, Y. Zhang, and J. Wang *et al.*, "Enhanced frequency-constrained unit commitment considering variable-droop frequency control from converter-based generator," *IEEE Transactions on Power Systems*, vol. 38, no. 2, pp. 1094-1110, Mar. 2023.

[14] M. Guan, "Scheduled power control and autonomous energy control of grid-connected energy storage system (ESS) with virtual synchronous generator and primary frequency regulation capabilities," *IEEE Transactions on Power Systems*, vol. 37, no. 2, pp. 942-954, Mar. 2022.

[15] M. M. Elwakil, H. M. E. Zoghaby, and S. M. Sharaf *et al.*, "Adaptive virtual synchronous generator control using optimized bang-bang for Islanded microgrid stability improvement," *Protection and Control of Modern Power Systems*, vol. 8, no. 4, pp. 1-21, Oct. 2023.

[16] V. Knap, S. K. Chaudhary, and D. I. Stroe *et al.*, "Sizing of an energy storage system for grid inertial response and primary frequency reserve," *IEEE Transactions on Power Systems*, vol. 31, no. 5, pp. 3447-3456, Sept. 2016.

[17] S. Yan, Y. Zheng, and D. J. Hill, "Frequency constrained optimal siting and sizing of energy storage," *IEEE Access*, vol. 7, pp. 91785-91798, Jul. 2019.

[18] A. Bera, B. R. Chalamala, and R. H. Byrne *et al.*, "Sizing of energy storage for grid inertial support in presence of renewable energy," *IEEE Transactions on Power Systems*, vol. 37, no. 5, pp. 3769-3778, Sept. 2022.

[19] F. Paganini and E. Mallada, "Global analysis of synchronization performance for power systems: bridging the theory-practice gap," *IEEE Transactions on Automatic Control*, vol. 65, no. 7, pp. 3007-3022, Jul. 2020.

[20] B. K. Poolla, S. Bolognani, and F. Dörfler, "Optimal placement of virtual inertia in power grids," *IEEE Transactions on Automatic Control*, vol. 62, no. 12, pp. 6209-6220, Dec. 2017.

[21] L. Pagnier and P. Jacquod, "Optimal placement of inertia and primary control: a matrix perturbation theory approach," *IEEE Access*, vol. 7, pp. 145889-145900, Oct. 2019.

[22] T. Borsche and F. Dörfler, (2017, May), "On placement of synthetic inertia with explicit time-domain constraints," arXiv preprint arXiv:1705.03244, [Online]. Available: https://arxiv.org/pdf/1705.03244

[23] H. Golpîra, A. Atarodi, and S. Amini *et al.*, "Optimal energy storage system-based virtual inertia placement: a frequency stability point of view," *IEEE Transactions on Power Systems*, vol. 35, no. 6, pp. 4824-4835, Nov. 2020.

[24] J. Rocabert, R. Capó-Misut, and R. S. Muñoz-Aguilar *et al.*, "Control of energy storage system integrating electrochemical batteries and supercapacitors for grid-connected applications," *IEEE Transactions on Industry Applications*, vol. 55, no. 2, pp. 1853-1862, Mar. 2019.

[25] T. Rahimi, L. Ding, and M. Kheshti *et al.* , "Inertia response coordination strategy of wind generators and hybrid energy storage and operation cost-based multi-objective optimizing of frequency control parameters," *IEEE Access*, vol. 9, pp. 74684-74702, May 2021.

[26] S. Rasool, K. M. Muttaqi, and D. Sutanto, "A multi-filter based dynamic power sharing control for a hybrid energy storage system integrated to a wave energy converter for output power smoothing," *IEEE Transactions on Sustainable Energy*, vol. 13, no. 3, pp. 1693-1706, Jul. 2022.

[27] H. Gao, P. Zi, and L. Huang *et al.*, "Optimal frequency control of grid-connected power electronic devices with energy constraints," *Automation of Electric Power Systems*, vol. 44, no. 17, pp. 9-18, Sept. 2020. (in Chinese)

[28] S. Wu, F. Liu, and Z. Wang *et al.*, "Minimum energy demands of energy storages for fast frequency response: formulation, solution, and implementation," *IEEE Transactions on Power Systems*, vol. 39, no. 2, pp. 3615-3630, Mar. 2024.

[29] U. Akram, M. Nadarajah, and R. Shah *et al.*, "A review on rapid responsive energy storage technologies for frequency regulation in modern power systems," *Renewable and Sustainable Energy Reviews*, vol. 120, Mar. 2020.

[30] K. Purchala, L. Meeus, and D. Van Dommelen *et al.*, "Usefulness of DC power flow for active power flow analysis," in *IEEE Power Engineering Society General Meeting*, San Francisco, USA, Jun. 2005, pp. 454-459.

[31] T. Ishizaki, A. Chakrabortty, and J. I. Imura, "Graph-theoretic analysis of power systems," *Proceedings of the IEEE*, vol. 106, no. 5, pp. 931-952, May 2018.

[32] RG-CE System Protection & Dynamics Sub Group (20 16, Mar.), "Frequency stability evaluation criteria for t he synchronous zone of continental europe-requirement s and impacting factors," ENTSO-E, Brusels, Belgium [Online]. Available: https://eepublicdownloads.entsoe.eu/clean-documents/SOC%20documents/RGCE_SPD_frequency_stability_criteria_v10.pdf

[33] A. Arana, J. Billo, and G. Chmiel *et al.*, (2020, Mar.), "Fast frequency response concepts and bulk power system reliability needs," North American Electric Reliability Corp. (NERC), Atlanta, GA [Online]. Available: https://pdf4pro.com/view/fast-frequency-response-concepts-and-bulk-power-system-79cdd0.html

[34] T. S. Borsche, T. Liu, and D. J. Hill, "Effects of rotational inertia on power system damping and frequency transients," in *2015 54th IEEE Conference on Decision and Control* (CDC), Osaka, Japan, Dec. 2015, pp. 5940-5946.

[35] M. Gibbard and D. Vowles (2014, Feb.), "Simplified 14-generator model of the south east Australian power syst em, revision 3", The University of Adelaide, South Aust ralia [Online]. Available: http://www.eleceng.adelaide.edu.au/groups/PCON/PowerSystems/IEEE/BenchmarkData/Simplified_14-Gen_System_Rev3_20100701.pdf

[36] C. Canizares, T. Fernandes, and E. Geraldi *et al.*, "Benchmark models for the analysis and control of small-signal oscillatory dynamics in power systems," *IEEE Transactions on Power Systems*, vol. 32, no. 1, pp. 715-722, Jan. 2017.